OPTICS

Amplified narrowband perovskite photodetectors enabled by independent multiplication layers for anti-interference light detection

Yao Ma[1], Xinglu Xu[1], Tengfei Li[2], Zemin Wang[2], Nan Li[2], Xin Zhao[1], Wei Wei[1], Xiaowei Zhan[2]*, Liang Shen[1]*

Metal-halide perovskite narrowband photodetectors offer a low-cost opportunity to detect specific signals covering a broad spectrum directly. However, the thickness of charge collection narrowing mechanism photodetectors increases recombination, resulting in performance bottlenecks. Here, we demonstrate amplified narrowband photodetectors that combine perovskite single-crystal absorbers and organic multiplication layers. The separation of the multiplication layer controls the density of trap states while amplifying the response of conventional narrowband photodetectors by more than 215 times. The carrier dynamics were characterized by ultrafast measurement, thus verifying the mechanism of response amplification. By analyzing multiplication with different trap states energy levels under charge injection, it is shown that dopants have a wide selection space, providing a feasible path for high-performance narrowband photodetectors. As a result, the external quantum efficiency of 2259% with a 38-nanometer full width at half maximum and the specific detectivity of 4.84 × 10^{12} Jones was obtained at 825 nanometers. Last, we demonstrated the anti-interference signal acquisition capability of our photodetector.

INTRODUCTION

Responding to specific wavelengths is widely needed in fluorescence imaging and detection, information encryption and anti-counterfeiting, and communications fields (*1*–*4*), which is currently achieved by broadband photodetectors combined with optical filters (*5*, *6*). However, the use of optical filters not only increases the complexity and cost of system integration but also affects the optical transmittance. At present, researchers have developed a variety of strategies to achieve narrowband detection based on organic and inorganic materials, including narrowband absorbing materials, charge collection narrowing, exciton dissociation narrowing, and light management (*7*–*10*). The charge collection narrowing mechanism is to selectively collect long-wavelength photogenerated carriers by using the difference between the length of carrier drift and the depth of light penetration to realize a narrowband response at the absorption cutoff edge of active material, which has been widely applied in various materials.

Metal-halide perovskites exhibit excellent performance in photovoltaic, light-emitting diode (LED), and photodetector fields, and the charge collection narrowing mechanism has been successfully introduced to fabricate perovskite narrowband photodetectors. Because of its easily tunable bandgap, narrowband detection coverage over a wide wavelength range can be achieved by changing its composition. Lin and colleagues demonstrated a set of narrowband red, green, and blue photodetectors based on perovskite with a full width at half maximum (FWHM) of less than 100 nm (*11*). Fang and colleagues present hybrid perovskite single-crystal narrowband photodetectors with an FWHM of less than 20 nm whose response spectra are continuously tuned from blue to red (*12*). Wang and colleagues reported a defect-assisted self-driven perovskite narrowband photodetector. By adjusting the halide component, a wide response range from red to near-infrared with FWHMs below 30 nm was shown, which is enabled by a thick perovskite film (*13*). To satisfy the annihilation of short-wavelength photogenerated carriers, the absorption layer thickness of the device far exceeds the diffusion length of carriers, resulting in a weak response. Although increasing bias voltage can improve carrier extraction, short-wavelength photogenerated carriers will contribute to photocurrent with increasing bias voltage, resulting in the degradation of the narrowband phenomenon. The researchers introduced dopants into the narrowband absorption layer to obtain gain, thereby improving the response. However, the response peak of most narrowband detectors in research comes from doped materials, which limits the tunability of the detection wavelength. In addition, introducing dopants into the absorption layer makes it difficult to control the concentration of trap states, thus being unable to reduce the impact on device performance.

Herein, we report amplified narrowband photodetectors (ANPDs) combining perovskite thin single crystals and organic multiplication trap layers. The photodetector separates the long-wavelength photogenerated electrons through the perovskite and drifts them into the multiplication trap layer under the bias voltage. After the photogenerated carriers are trapped by fused-ring electron acceptor dopants, the energy band is bent, and current tunneling injection is formed. By separating the multiplication layer from the light absorption layer, the distribution and density of trap states can be controlled, thereby reducing the negative impact of trap states on performance. Through a series of ultrafast photoelectric characterizations, we prove that the source of gain of ANPDs is current injection caused by trapped electrons in multiplication layers. We introduced various fused-ring electron acceptors as dopants to construct different types of traps and demonstrated that under carrier injection, type II heterojunctions can also form effective charge traps. As a result, ANPDs obtained a narrowband external quantum efficiency (EQE) response of 2259% at 825 nm with an FWHM of 38 nm, which is 215 times

[1]State Key Laboratory of Integrated Optoelectronics, College of Electronic Science and Engineering, International Center of Future Science, Jilin University, Changchun, People's Republic of China. [2]State Key Laboratory of Advanced Waterproof Materials, School of Materials Science and Engineering, Peking University, Beijing 100871, P. R. China.
*Corresponding author. Email: shenliang@jlu.edu.cn (L.S.); xwzhan@pku.edu.cn (X.Z.)

higher than that of the basic perovskite single-crystal narrowband photodetector. The anti-interference ability of the ANPDs has been further analyzed by capturing target signals under different light interferences, providing a promising way to improve the response capability of perovskite single-crystal narrowband detectors.

RESULTS

Amplified narrowband photodetectors

On the order of the Beer-Lambert Law, light with short wavelengths can penetrate only a short distance through the absorbing layer, whereas longer wavelengths require thicker materials to be fully absorbed. Therefore, short-wavelength light only generates charge carriers near the surface, whereas long-wavelength light can generate carriers inside the crystal (*14*). By controlling the thickness of the active layer, photogenerated carriers at the absorption cutoff edge of the material (long-wavelength light) can be selected as the only source contributing to the photocurrent, thus realizing narrowband photoelectric response, with the charge collection narrowing mechanism (Fig. 1A). To enhance response, the multiplication layer is constructed by organic materials on top of the perovskite narrowband response layer. By mixing organic materials in large proportion differences so that the doped materials are not continuously distributed in the bulk material, electron or hole traps can be constructed according to the band structure. As shown in Fig. 1B, under dark conditions, the higher work function of the silver electrode makes it difficult for holes to cross the energy barrier and inject into the device. Thus, the blocked carrier injection results in a small dark current. Under illumination, the electrons generated by long-wavelength light in the perovskite absorption layer can drift into the multiplication layer under the bias voltage and then be trapped by electron traps. Because of the negative charged traps, the energy band of the organic layer bends downward, thereby narrowing the energy barrier of Schottky junctions, and holes can tunnel into the device, bringing photocurrent gain (*15*).

To demonstrate the response amplification effect of adding the organic multiplication layer to perovskite narrowband detectors, we choose the well-studied $MAPbI_3$ single crystal as an example. $MAPbI_3$ thin single crystals were grown using the previously reported space confinement method (*16*). Using polytetrafluoroethylene as a spacer to control thickness, crystals with a thickness of ~500 μm were grown on the poly[bis(4-phenyl)(2,4,6-trimethylphenyl)amine] (PTAA)–coated indium tin oxide (ITO) substrate. After depositing the C_{60} and electrode, narrowband photodetectors were fabricated. On the order of the energy band of $MAPbI_3$, PTB7-Th is chosen as the bulk material of the multiplication layer according to the requirement of energy level matching (Fig. 1C) (*17*). The selection of dopants needs to meet two requirements: First, they can match the band structure of the bulk material and form effective charge traps; second, their light absorption or response cannot disrupt the narrowband phenomenon of the photodetector. Because of their low nonradiative recombination, adjustable energy level, and ability to passivate perovskite defects, narrow bandgap fused-ring electron acceptors are selected as dopants to construct charge traps (*18*). The energy level difference of 0.11 eV between the lowest unoccupied molecular orbital (LUMO) of PTB7-Th and the conduction band minimum (CBM) of perovskite does not have a fatal effect on electron transport under bias voltage, whereas the LUMO difference between PTB7-Th and COTIC-4F is 0.52 eV so that electron traps can be formed (Fig. 1D). In this band alignment, the gain from the organic layer becomes achievable.

Characterization of amplified narrowband response

The EQE of the perovskite narrowband photodetectors is shown in Fig. 2A, which exhibits a narrow response peak at around 825 nm. Similar to the results in previous reports, with the increase in bias

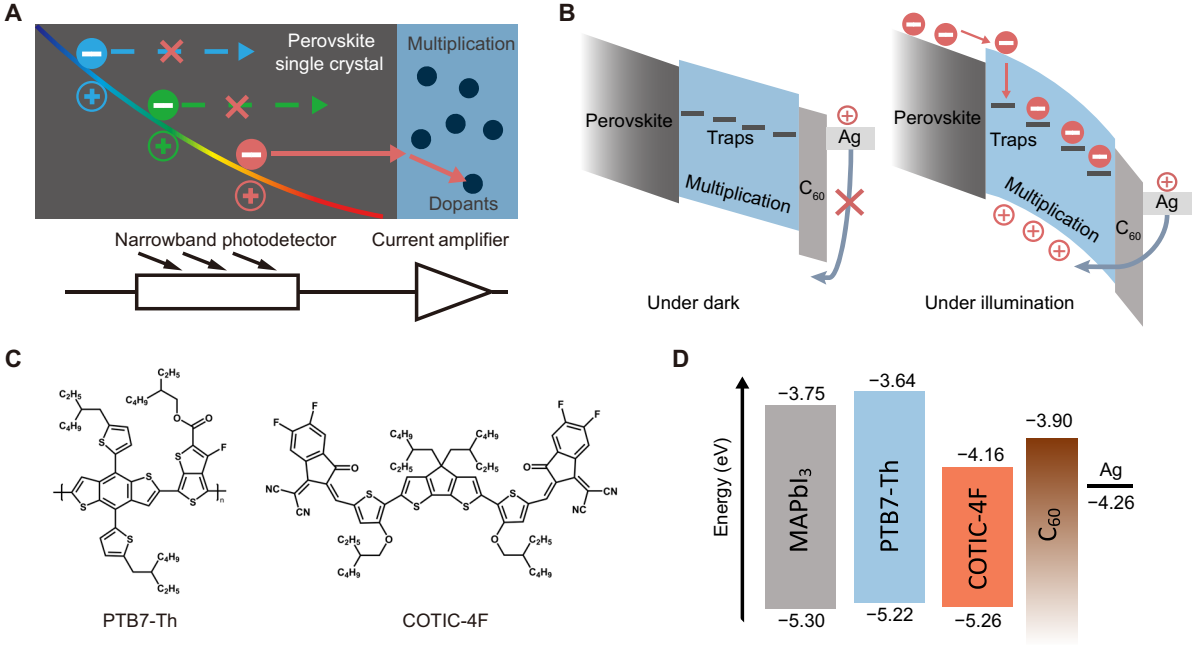

Fig. 1. Schematic diagram of ANPDs. (**A**) Schematic diagram of the ANPD structure and narrowband detection mechanism. Only long-wavelength photogenerated carriers can be injected into the organic multiplication layer. (**B**) Working mechanism of the organic multiplication layer. After the injected electrons are trapped, hole injection is induced. (**C**) Molecular structures of PTB7-Th and COTIC-4F. (**D**) Energy level structures of perovskite and organic materials.

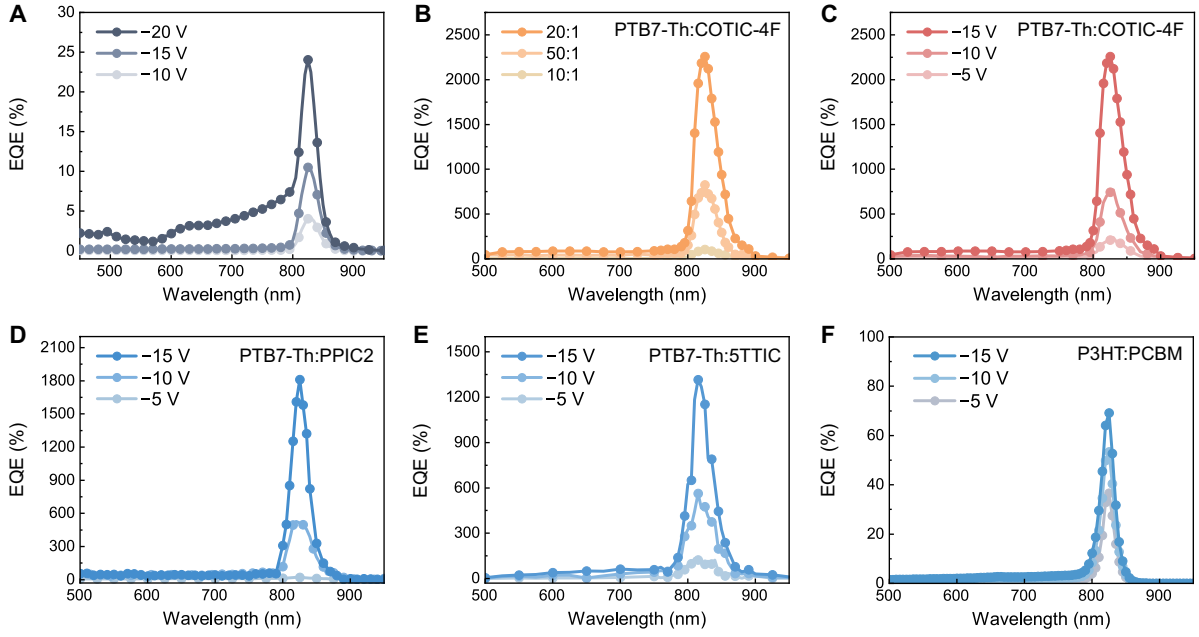

Fig. 2. Response characteristics of different narrowband photodetectors. (**A**) EQE response of perovskite single-crystal narrowband photodetectors at different bias voltages. The device loses its good narrowband response at −20-V bias. (**B**) EQE response of ANPDs at different organic multiplication layer doping ratios. (**C**) EQE response of 20:1 mass ratio doped ANPDs at different voltages. (**D** to **F**) ANPDs with different trap states were constructed using PTB7-Th:PPIC2 (D), PTB7-Th:5TTIC (E), and P3HT:PCBM (F).

voltage, the narrow response peak increases gradually, but the narrowband phenomenon has also been destroyed under large bias, that is, the short-wavelength photogenerated carriers gradually pass through the whole crystal (*12*). Under −20-V bias, the response from around 600 to 800 nm starts to rise, which limits how the EQE can be improved by increasing the operating bias voltage.

To prepare the organic multiplication layer, PTB7-Th and COTIC-4F were dissolved in chlorobenzene at mass ratios of 50:1, 20:1, and 10:1 and were fabricated on perovskite by the same spin-coating process (fig. S1). Figure 2B shows the EQE of ANPDs with three different dopant concentrations and the multiplication layer where the 20:1 mass ratio exhibits a notable advantage. After fabricating the multiplication layer, the position of the narrowband response peak does not change notably. The enlarged EQE results for the ANPDs with the mass ratio of 50:1 and 10:1 are shown in fig. S2. The multiplication effect hardly appears in the device with the 10:1 mixing ratio, with the maximum EQE still not exceeding 100%. This may be due to the continuous distribution of excessive dopants, carriers can be directly transported in the dopants, and effective electron traps cannot be formed. Although the 50:1 doped detector exhibits a multiplication effect with the EQE exceeding 600%, the response amplification is far inferior to that of the 20:1 doped device. Thicker perovskite single-crystal materials bring less electron injection, so more traps are needed to achieve sufficient band bending. We analyzed the voltage dependence of the multiplication effect, and the results are shown in Fig. 2C and fig. S3. At low bias voltage, the ANPDs do not exhibit a multiplication effect, similar to that of normal narrowband detectors. This is mainly due to the strong correlation between the probability of trap-induced hole injection and bias voltage (*19*). With the increase in voltage, the multiplication effect appears obviously. At −15-V bias, the EQE of the ANPDs exceeds 2259%, with an FWHM of 38 nm, which is more than 215 times higher than that of the conventional narrowband perovskite photodetector. As the light intensity increases, the trap filling gradually saturates, corresponding to a reduced multiplication, as shown in fig. S4. By adjusting the spin-coating speed, the EQE results of devices with different organic layer thicknesses were carried out in fig. S5. A higher spin-coating speed leads to an inevitable decrease in EQE, mainly due to the thin organic layer potentially not being able to fully cover the surface of the perovskite, resulting in direct contact between the transport layer and the perovskite. In this case, the organic layer is unable to efficiently capture electrons, thus weakening the multiplication effect. This is consistent with our illustrated mechanism. When the spin-coating speed decreases, the thick organic layer affects the transport of charge carriers, improves recombination, and reduces the EQE. Although the response is amplified, the narrowband effect is not notably affected.

In addition, the EQE shows no response peaks other than those of $MAPbI_3$ but only a slight broadening of the FWHM (from 33 nm for perovskite narrowband detectors to 38 nm). Although the bandgap of $MAPbI_3$ is about 1.55 eV, indirect bandgap absorption of single crystal extends the photoresponse range into the near-infrared region (*20*). Compared with 1.3-μm-thick $MAPbI_3$ polycrystalline films, the absorption cutoff edge of the 500-μm-thick single crystal redshifts from about 780 nm to more than 850 nm (fig. S6A). Because the absorption range of PTB7-Th is narrower than that of perovskite with a thickness of 500 μm, PTB7-Th is almost unable to effectively absorb light (fig. S6B). The bandgap of COTIC-4F is smaller than $MAPbI_3$, but there are no other response peaks in the infrared region. There are two main reasons why the ANPD does not show a notable response to the long-wavelength portion of the incoming light. The defects in perovskite introduce relatively complex

energy levels in the forbidden band, thus bringing about the absorption band tail (*21*, *22*). The absorption beyond the EQE tail due to these energy disturbances cannot efficiently generate free carriers and the absorption coefficient is low, but it still has a considerable effect on infrared transmission at thicker crystal sizes. The incident light first passes through the perovskite crystal region and is absorbed, so less long-wavelength light enters the organic layer. We tested the transmittance of the $MAPbI_3$ crystal about 500 μm thick, and fig. S6C shows that the maximum transmission beyond 900 nm is less than 11%. In addition, the normalized absorption of the organic multiplication layer, PTB7-Th, and COTIC-4F are shown in fig. S6 (A and C). Although the acceptor in the organic layer has a small bandgap so that its absorption range covers the long-wavelength band, because of the small doping ratio, the absorption of the prepared organic layer film is very weak after 850 nm (fig. S6C). Combined with the above two factors, the acceptor material in the organic layer is difficult to effectively absorb the long-wavelength light. Second, because of the small doping proportion, acceptor materials appear as discontinuous isolated states. Combined with the energy band structure of PTB7-Th, the carrier generated in COTIC-4F is difficult to separate, which affects the carrier collection. On the order of the same process, the organic multiplication layer (PTB7-Th and COTIC-4F, mass ratio of 20:1) is selected to prepare an organic photodetector. The blue curves in fig. S7 shows the EQE results of the organic device under different bias voltages, which did not exhibit notable carrier collection beyond 850 nm. Furthermore, the EQE of the organic device under −8 V at 825 nm is only 2.6%, which is much lower than the peak EQE of 216% at 475 nm. Because only about 3.5% of the 825-nm light can penetrate the perovskite crystal and reach the organic layer (fig. S6B), the light absorption of the organic layer would not make a notable contribution to the EQE of ANPDs.

The selection of dopants needs to meet the dual requirements of narrowband detection and multiplication. Compared to PTB7-Th, the low LUMO and highest occupied molecular orbital (HOMO) of COTIC-4F introduce only electron traps into the organic layer, but this strict energy level alignment limits the range of dopant selection. Therefore, two narrow bandgap organic materials are tested to verify whether this amplification structure has a wider selection of dopants. The EQE results without detailed optimization are shown in Fig. 2 (D and E), and the band alignments are shown in fig. S8 (A and B), in which the HOMO of PPIC2 (*23*) and 5TTIC (*24*) is higher than PTB7-Th. Higher HOMO results in weaker exciton separation capabilities, which can help reduce the extra response peaks due to the dopant's absorption. However, the HOMO difference of 5TTIC (0.07 eV) and PPIC2 (0.13 eV) not only strengthens the suppression of exciton dissociation but also challenges the electron trapping ability of electron traps. The EQE curves in Fig. 2 (D and E) show that, when the free carriers in the multiplication layer are mainly perovskite injected electrons, the trapping ability and trap charge lifetime of the electron traps are not fatally affected, showing good multiplication ability. It is worth noting that, in the 850- to 900-nm wavelength range, the EQE response of ANPDs with PPIC2 and 5TTIC is better suppressed compared to ANPD with COTIC-4F, which can be attributed to the failure of exciton dissociation. Last, we used dopants with lower HOMO energy levels to construct ANPDs (fig. S8C). FOIC (*25*) forms a good heterojunction with PTB7-Th and can effectively separate photogenerated excitons, but its bandgap of about 1.44 eV coincides with the response peak of $MAPbI_3$. Because of the high absorption coefficient of perovskite within the bandgap, fig. S6B indicates that there is almost no light passing through the crystal, so it will not affect the narrowband phenomenon (fig. S8D). Although the LUMO levels of these materials are higher than COTIC-4F and can affect the lifetime of trapped electrons, EQE results show that small LUMO level changes do not have a notable impact. To sum up, this multiplication structure offers wide selections of dopants, and various energy level alignments can be used. This provides a good basis for the ANPD structure to be applied to different perovskite compositions for different wavelengths.

To verify that the response of ANPDs is derived from light absorption by perovskites, rather than organic layers, fig. S9 shows the relationship between the EQE of the narrowband photodetectors and the absorption of various acceptor materials. The above figure shows the narrowband EQE result of pure $MAPbI_3$ devices and the absorption curve of $MAPbI_3$. It can be seen that the response peak of around 825 nm is located at the absorption cutoff edge of perovskite. The middle and the bottom figures show the absorption curves of COTIC-4F and PPIC2 and the EQE results of the corresponding ANPDs. It can be seen that the EQE of the detectors is not located at the absorption cutoff edge of the acceptor materials but is located near 825 nm as the peak EQE of the perovskite device. The P3HT:PCBM and PTB7-Th:PCBM organic multiplication layers are constructed to avoid the influence of organic materials absorption at 825 nm, and the energy band structures are shown in fig. S10. As shown in Fig. 2F, although the LUMO energy level of P3HT hinders the transport of electrons from perovskite to the organic layer, the EQE at about 825 nm has still been improved compared to perovskite narrowband photodetectors. Combined with the results in fig. S10C, it suggests that the response of the ANPD is derived from the absorption of perovskite rather than the absorption of the organic layer.

Ultrafast characterization of carrier dynamics in absorption and multiplication regions

To verify the mechanism of narrowband response amplification, we characterize the charge transfer between the perovskite absorption layer and the organic multiplication layer by femtosecond transient absorption (TA) measurement (*26*–*28*), and $MAPbI_3$ polycrystalline thin films were prepared by the spin-coating method to simulate the interface, with multiplication layers prepared on the perovskite films. Because the indirect bandgap absorption coefficient of perovskite is small, the sub-bandgap absorption of the thin film is weak, showing the band edge absorption at around 780 nm, but the energy band structure of perovskite thin films and single crystals is similar (*20*). To study the carrier dynamics under the influence of bias voltage, the device structure is ITO/poly(methyl methacrylate) (PMMA)/absorption layer/bathocuproine (BCP)/Au, as shown in fig. S11. The active layer is separated from the electrode by PMMA and 50-nm-thick BCP to avoid carrier extraction. The TA spectrums of perovskite and perovskite/organic devices were measured by using a 515-nm femtosecond laser incident from the perovskite side as pump light (Fig. 3, A and B). The negative absorption signal at about 750 nm is attributed to the ground state bleaching (GSB) signal of $MAPbI_3$, that is, the transition from the valance band maximum (VBM) to the CBM after carriers absorb photons. The positive absorption signal at 775 nm is attributed to the excited state absorption (ESA) of $MAPbI_3$, that is, the transition of excited state carriers to higher energy levels (*29*). Both perovskite devices and perovskite/organic devices show that these two characteristic peaks and the positions are not deviated. In addition to the two characteristic peaks attributed to perovskite, the TA plots of perovskite/organic devices exhibit additional negative absorption signals in the 630- to 700-nm and 800- to 900-nm ranges.

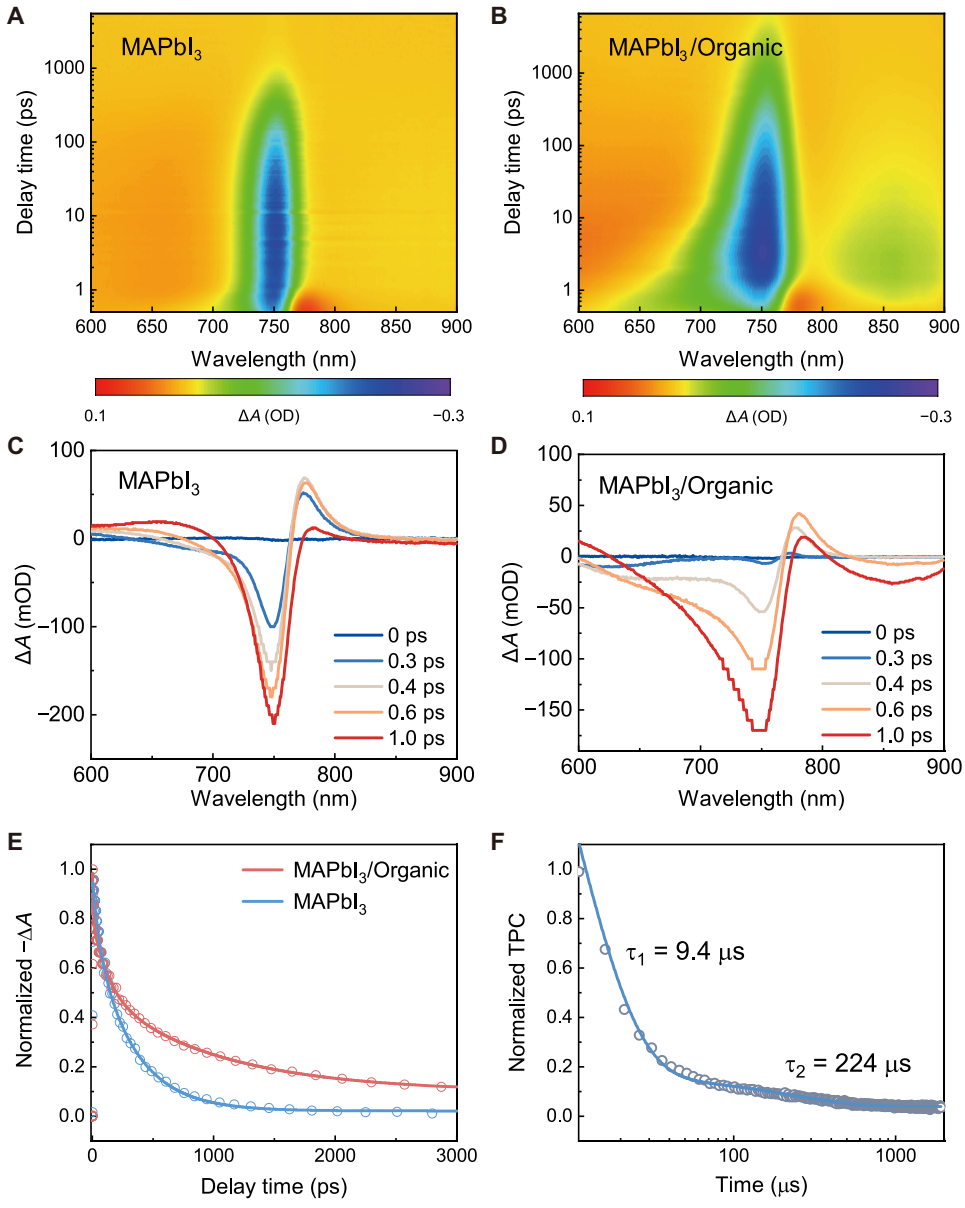

Fig. 3. Ultrafast measurements for active layer films and ANPDs. (**A** and **B**) Time-wavelength–dependent TA color maps of the $MAPbI_3$ device (A) and $MAPbI_3$/Organic device (B). OD, optical density. (**C** and **D**) TA spectrum at selected timescales of the $MAPbI_3$ device (C) and $MAPbI_3$/Organic device (D). (**E**) TA spectra at 750 nm as a function of delay time. (**F**) TPC characterization and second-order exponential fitting of ANPDs.

Figure 3 (C and D) shows a more detailed comparison of the carrier dynamics of the two devices. On the order of the absorption curves of PTB7-Th and COTIC-4F shown in fig. S6A, the negative signal from 600 to 700 nm is mainly attributed to PTB7-Th (*30*). At 0.3 ps, PTB7-Th and $MAPbI_3$ have the same negative signal intensity, but with time, the $MAPbI_3$ signal gradually drowns the PTB7-Th signal. To determine the source of the negative signal from 800 to 900 nm, we tested the photoluminescence (PL) curve of the perovskite film as shown in fig. S12. The PL peak of $MAPbI_3$ is before 800 nm, so the negative signal in this range should be mainly attributed to COTIC-4F. Because the absorption of COTIC-4F at 515 nm is very weak, it will not be pumped to produce a notable negative signal. Although PTB7-Th is excited by the 515-nm pump light at 0.3 ps, no negative signal is generated at 850 nm. At 0.6 ps, the negative signal of $MAPbI_3$ at 750 nm has completely covered the PTB7-Th signal, and then the negative signal at 850 nm appears, which indicates that the negative signal at this time comes from the injection of carriers in the perovskite into the organic layer under the action of bias voltage (*31*). To prove this, we fabricated devices with only organic layers, where the carriers generated in PTB7-Th cannot produce a sufficient signal at 850 nm (fig. S13). Besides, the rising of the 750- and 850-nm signal of perovskite/organic devices is shown in fig. S14. The rise of the 750-nm signal shows three stages: fast rise, slow rise, and fast rise. The slow rising phase matches with the rising process of the 850-nm signal, which also proves the source of the 850-nm signal. Figure 3E fits the decay process of the normalized GSB signal at 750 nm of the two

devices. The average decay time of perovskite devices is 309 ps, whereas the decay time is extended to 911 ps after adding the organic layer, indicating that ground state carriers need a longer time to be replenished. In contrast to the second-order fit lifetime of the perovskite device, the third-order fit lifetime of the perovskite/organic device indicates that there is an additional recombination path, which is recombination after charge transfer.

Transient photocurrent (TPC) and transient photovoltage (TPV) measurements were performed on ANPDs to characterize the trapping process of electrons entering the organic multiplication layer (*32*–*35*). The TPC, which characterizes the dynamics of carrier extraction in the device, is shown in Fig. 3F. The fitting curve contains fast decay (9.4 μs) and slow decay (224 μs), in which the fast component is the main process, which is mainly attributed to the transit and extraction of free electrons generated in $MAPbI_3$ under the bias voltage. The slow decay time indicates the presence of traps in the device, whereas the detrapping time notably prolongs the TPC lifetime. In addition, the second-order fitting TPV results in fig. S15 indicates the presence of two recombination channels, which are consistent with the TPC results and jointly confirm the existence of trap states. The space charge limiting current (SCLC) method is applied to the organic multiplication layer to identify the type of charge trap (*36*, *37*), as shown in fig. S16 (A and B). The hole trap density and electron trap density in the multiplication layer are calculated by preparing hole-only and electron-only devices. The density of hole traps and electron traps is 5.2×10^{15} and 6.3×10^{17} cm^{-3}, which is more than two orders of magnitude of the former, which indicates that the doping of COTIC-4F successfully introduces electron traps and thus produces the multiplication effect. In addition, to verify that the introduction of organic layers controls the concentration of trap states in ANPDs, SCLC measurements were also conducted on perovskite/organic devices (fig. S16, C and D). The densities of hole traps and electron traps are 3.4×10^{10} and 8.5×10^{10} cm^{-3}, which is consistent with the concentration of defect states in perovskite single crystals (*38*–*40*). In conclusion, when the long-wavelength generated electrons drift to the interface between perovskite and organic multiplication layer under the bias voltage, the free electrons enter the multiplication layer and are captured by the electron traps formed by PTB7-Th and COTIC-4F, thus bringing the multiplication effect.

Other key performances of ANPDs

The current-voltage curves of the ANPDs based on the 20:1 mass ratio multiplication layer under dark conditions and 850-nm illumination are shown in Fig. 4A. The dark current of the device does not increase sharply with the increase in bias, but the photocurrent shows an obvious increase at about −9 V, at which a large number of holes at the interface begin to tunnel. From the rapid rise of photocurrent, the ANPDs enter into the multiplication region, and the on-off ratio threshold voltage is consistent with the results of EQE, that is, the multiplication phenomenon is not obvious at low bias. The dark current and photocurrent of the perovskite single-crystal narrowband photodetector and the organic photodetector under the same conditions are shown in fig. S17. The weak absorption of organic photodetectors in the infrared band makes it difficult to obtain sufficient response, once again indicating that the photocurrent amplification of ANPDs in the infrared band is derived from the injection of photogenerated electrons from perovskite

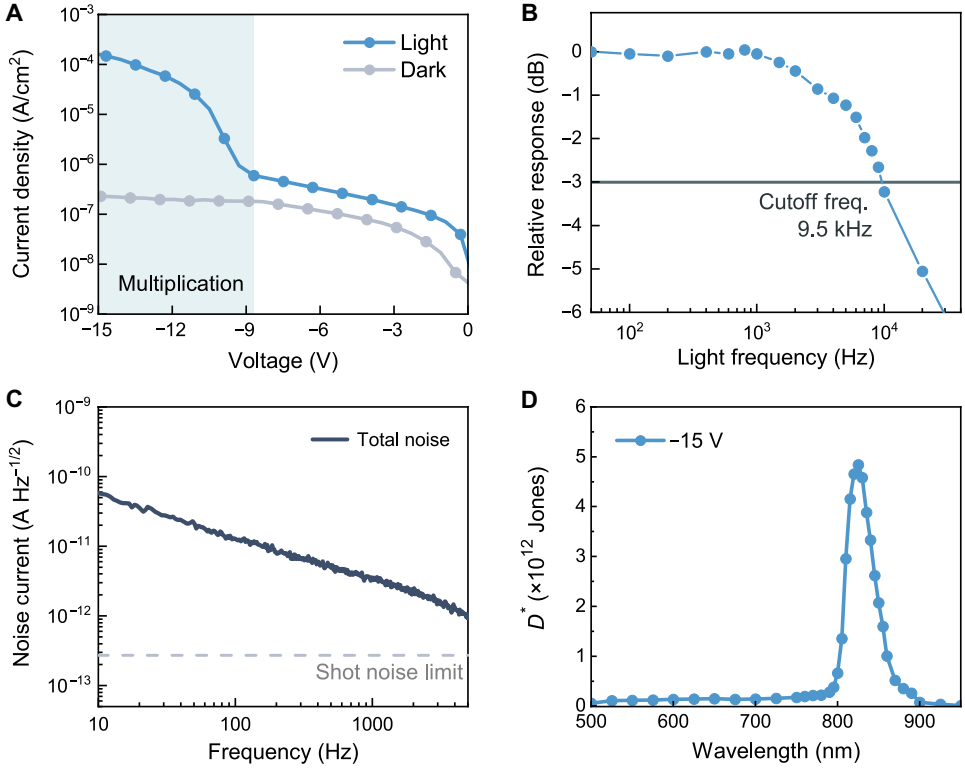

Fig. 4. Device performances of ANPDs. (**A**) Dark current and photocurrent of ANPDs under 850-nm illumination of 0.04 mW cm^{-2}. (**B**) Relative response as a function of light frequency showing the −3-dB cutoff frequency; the detector operates under a voltage of −15 V and a light intensity of 130 μW cm^{-2}. (**C**) Measured total noise current and shot noise limit under −15 V. (**D**) Specific detectivity of ANPDs under −15 V.

single crystals into the organic layer. The effect of the trap states in the organic layer on carrier dynamics under light conditions is analyzed by the Fowler-Nordheim (FN) plots, which are obtained from the current-voltage curves (*41*). The linear decrease curve under light conditions shown in fig. S18A shows that the FN tunneling effect plays a major role in ANPDs at high voltage. In contrast, the same decrease is not seen in the perovskite photodetector under light conditions (fig. S18B), indicating that FN tunneling is attributed to the organic layer, which is consistent with the tunneling mechanism shown in Fig. 1B. Because the trap effect can greatly affect the response speed of the photodetector, the frequency response characteristics are performed. By adjusting the frequency of the 850-nm light source and collecting the response signal (*42*, *43*), the −3-dB cutoff frequency of ANPDs is obtained beyond 9.5 kHz (Fig. 4B). The cutoff frequency of the photodetector without a multiplication layer was carried out in fig. S19, indicating that our detector has a well-balanced response multiplication and speed attenuation. In addition, we characterized the response time of the photodetector, with a rise time of 82 μs and a decay time of 86 μs (fig. S20). The noise current of ANPDs is directly measured at −15 V, as shown in Fig. 4C. Compared with the theoretical shot noise limit calculated by dark current, the total noise spectrum of the detector exhibits 1/f noise dominance and a large slope, which is related to the large number of electron traps in the organic multiplication layer (*44*). The responsivity curve calculated by the EQE is shown in fig. S21, and the peak value is 15 A/W at 825 nm. Combined with the frequency response characteristics of ANPDs, the specific detectivity (D^*) of the detector is calculated by using the noise current spectrum and responsivity (*45*). As shown in Fig. 4D, the ANPD exhibits a peak D^* of 4.84×10^{12} Jones. The excellent performance of the narrowband multiplication structure provides a solid foundation for the application of perovskite narrowband photodetectors. To characterize the response of the detector as a function of light intensity, fig. S22 exhibits that the photocurrent increased linearly with the light intensity from around 1.1×10^{-5} to 6.7 mW/cm^2, corresponding to an linear dynamic range (LDR) of 58 dB.

Anti-interference response measurements with ANPDs

Low-cost, high-response narrowband detectors have potential value in various application scenarios, such as the Internet of Things with lighting optical communication, information encryption, anti-counterfeiting using wavelength differences, fluorescence detection, and imaging (*46*–*49*). These applications have put forward high requirements for the anti-interference ability of photodetectors, namely, the signal-to-interference ratio (SIR). To verify the anti-interference ability of ANPDs, we built a measurement system as shown in Fig. 5A. By using a function signal generator, the target light and interference light are modulated to different frequencies and simultaneously irradiated onto the detector through

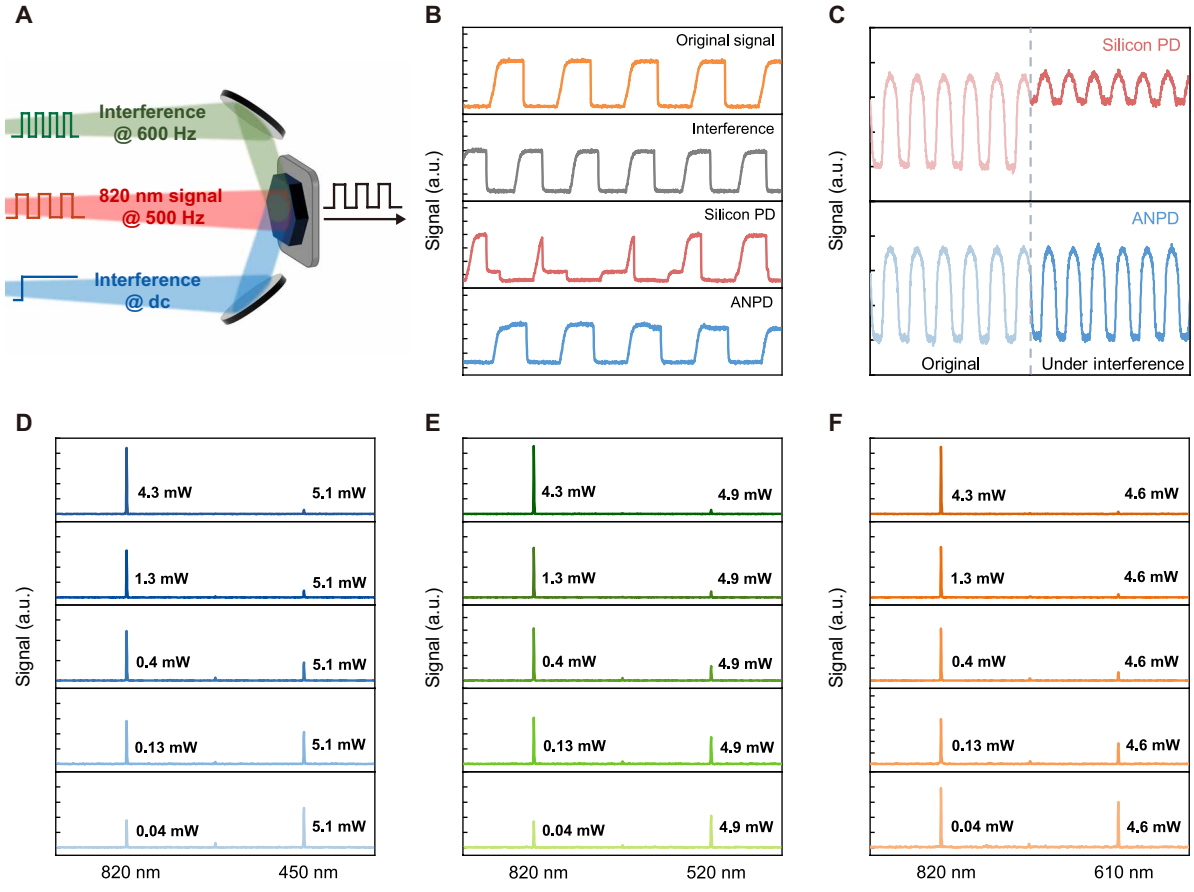

Fig. 5. Characterization of the anti-interference performance of ANPDs. (**A**) Schematic diagram of the measurement system setup. (**B**) Impact of interference light on the signal waveform obtained by silicon photodetectors and ANPDs. a.u., arbitrary units. (**C**) Impact of interference light on the signal amplitude obtained by silicon photodetectors and ANPDs. (**D** to **F**) Performance of ANPDs to suppress the interference light of 450 nm (D), 520 nm (E), and 610 nm (F). Keep the interference light intensity unchanged and gradually reduce the intensity of the 820-nm light. By modulating the light of different wavelengths to different frequencies and conducting spectral analysis, the contribution of different wavelengths of light to response can be obtained.

a lens group. Afterward, the collected detector signals are analyzed using an oscilloscope to characterize the anti-interference ability of the device. To eliminate the influence of frequency on the response of ANPDs, based on the −3-dB results, the 820-nm light is modulated to 500 Hz as the original signal, and the white light is modulated to 600 Hz as interference, as shown in Fig. 5B. Compared with the original signal, the electrical signal of the silicon detector is severely distorted and cannot obtain the information, whereas the signal of ANPDs is almost unaffected. This means that, in lighting optical communication, ANPDs can receive information transmitted by signal light without interference. In addition to the waveform, we analyzed the amplitude of the obtained signal. As shown in Fig. 5C, the light-colored curve on the left represents the original signal received by the silicon photodetector and ANPD, whereas the right is the signal after applying dc white interference light. Compared to silicon photodetectors with notably compressed signal amplitude, the signal amplitude of ANPDs remains almost unchanged.

To further characterize the SIR of ANPDs, we analyzed the frequency characteristics of the signal. By converting the read signal into the frequency domain, we can distinguish the contribution of light modulated at different frequencies to the total photocurrent of the detector. Figure 5 (D to F) shows the spectral analysis results of the ANPDs under three wavelengths of light interference. When the interference light has similar optical power to the target light, the device exhibits excellent interference suppression ability. By overlaying neutral density filters with different optical densities, we gradually reduce the intensity of the target light (820 nm) while maintaining the interference light. For blue (450 nm, 5.1 mW) and green (520 nm, 4.9 mW) interference light, the SIR of the 820-nm light at 133 μW is 2.21 and 4.56 dB (*50*, *51*). For orange interference light (610 nm, 4.6 mW), the SIR remains greater than 2.47 dB even after the target light power is reduced to 43 μW (two orders of magnitude smaller than the interference signal). The SIR fitted curve of ANPDs is shown in fig. S23. When the SIR is 0 dB, meaning that the signal borders on unreadable, the power of the 820-nm signal light has decreased to 0.57% (610 nm), 1.16% (520 nm), and 1.54% (450 nm) of the interference light. This indicates that, when the fluorescence emission intensity is much lower than the background light, ANPDs can still successfully capture the presence of fluorescence signals.

DISCUSSION

We have demonstrated a high-performance ANPD based on perovskite and organic materials. The separated organic multiplication layer can effectively control the overall trap state density of the device, thereby reducing the impact of trap effects on other performances. By using the tunable band structure of the fused-ring electron acceptor, various types of traps can be constructed based on it as a dopant, thereby verifying the wide compatibility of the device structure. The carrier dynamics characterized by TA, TPC, and TPV verify the injection of photogenerated carriers into the multiplication layer and the effect of charge traps in the multiplication layer on carriers. As a result, the amplification of the narrowband response of the photodetector is realized, and an EQE of more than 2259% with an FWHM of 38 nm is obtained. The ANPDs have a frequency characteristic exceeding 9.5 kHz and a D^* of 4.84×10^{12} Jones at 825 nm. Amplified narrowband structures provide a promising path for improving the performance of perovskite narrowband photodetectors covering multiple spectral bands.

MATERIALS AND METHODS

Growth of perovskite single crystals

Perovskite thin single crystals are grown through a space-confinement process that combines inverse temperature crystallization and solvent evaporation crystallization. PTAA toluene solution with a concentration of 2 mg/ml was spin coated on a precleaned ITO substrate at 4000 rpm, followed by annealing at 100°C for 10 min. The two substrates are bonded with silicone, and a certain solvent evaporation opening is retained. The thickness is controlled through a polytetrafluoroethylene film in the middle. Dissolve methylammonium iodide (MAI) and PbI_2 in γ-butyrolactone at a molar ratio of 1.1:1 and prepare as a precursor solution with a concentration of 1.2 M. After injecting the solution into the growth device, place it in an oven, raise the temperature to about 90°C, and evaporate the solvent until the seed crystals appear. Then, the temperature gradually increases at a rate of 0.5°C/hour until the crystal reaches the required size.

Device fabrication

For perovskite narrowband detectors, 20-nm C_{60} and 80-nm copper were prepared by vacuum thermal deposition on grown single crystals. For ANPDs, PTB7-Th and COTIC-4F, 5TTIC, PPIC2, and FOIC were doped in corresponding proportions and dissolved in a chlorobenzene solvent to prepare an organic solution with a concentration of 15 mg/ml. Next, spin coat the organic solution onto the surface of the single crystal at a speed of 800 rpm and then anneal at 100°C for 10 min. Last, 20-nm C_{60} and 80-nm silver electrodes were prepared by vacuum thermal deposition.

Device fabrication for TA measurement

PMMA is dissolved in *n*-butyl acetate at a mass concentration of 4% and stirred at 55°C until clear and transparent. Spin coat PMMA onto the ITO substrate at a speed of 2000 rpm and anneal at 120°C for 2 hours. Dissolve MAI and PbI_2 in a ratio of 1:1 in a mixed solvent of *N*,*N*′-dimethylformamide and dimethyl sulfoxide (9:1) and prepare a precursor solution of 0.75 M. According to the requirements, deposit the perovskite and organic multiplication layer and sequentially spin coat the perovskite and organic multiplication layer. Last, 50-nm BCP and 18-nm gold electrode were deposited by the vacuum thermal deposition method.

Ultrafast photoelectric characterization

The TA measurements were performed by a femtosecond laser and Time-tech Spectra TA100. Use a 515-nm laser as the pump light to irradiate the perovskite side while applying a negative voltage to the device. By using PMMA and BCP as insulation layers, the active layer is kept in an electric field environment without the extraction of charge carriers to simulate the carrier dynamics at the ANPD interface. Use a nanosecond laser, oscilloscope, and SR570 low-noise current amplifier to characterize the TPC and TPV of ANPDs.

Frequency response characterization

Under a dark environment, square wave signals are output to an 820-nm LED through a function generator, gradually modulating its frequency from low to high. The photocurrent obtained by the photodetector under LED illumination is amplified by an SR570 low-noise current amplifier and collected using a Keysight DSOX6004A Oscilloscope. The −3-dB cutoff frequency was obtained by calculating the relative response.

Characterization of the anti-interference ability

Using the signal generator of the Keysight DSOX6004A Oscilloscope, modulate the interference light at 450, 520, and 610 nm to 600 Hz and modulate the signal light at 820 nm to 500 Hz. Use a lens group to simultaneously illuminate two beams of light onto the photodetector and collect the output signal using an oscilloscope and a current amplifier. In signal amplitude measurement, modulate the interfering light to dc. In the SIR measurement, a set of neutral density filters is combined to gradually reduce the intensity of the signal light and verified using a Newport 843-R optical power meter. Analyze the impact of the two types of light on the detector response signal through a Keysight N9322C spectrum analyzer.

Other characterization

A Shimadzu UV-1700 Pharma Spec UV spectrophotometer was used to measure the absorption spectra. A Shimadzu RF 5301 fluorescence spectrophotometer was used to obtain the PL spectra of our devices. Scanning electron microscopy (SEM) measurements were carried out using a JSM-7900F. SCLC analysis was measured by Keysight 2901A source meter. The EQEs and transmittance were measured by a Crowntech Q test Station 1000 AD measurement system. The *J-V* curves of our photodetectors in the dark and under illumination were obtained by a Keithley 4200 semiconductor parameter analyzer. The noise current was analyzed by a ProPlus 9812D wafer level 1/f noise characterization system.

Supplementary Materials

This PDF file includes:

Figs. S1 to S23

REFERENCES AND NOTES

1. G. Konstantatos, J. Clifford, L. Levina, E. H. Sargent, Sensitive solution-processed visible-wavelength photodetectors. *Nat. Photonics* **1**, 531–534 (2007).
2. X. Gong, M. Tong, Y. Xia, W. Cai, J. S. Moon, Y. Cao, G. Yu, C.-L. Shieh, B. Nilsson, A. J. Heeger, High-detectivity polymer photodetectors with spectral response from 300 nm to 1450 nm. *Science* **325**, 1665–1667 (2009).
3. G. Konstantatos, E. H. Sargent, Nanostructured materials for photon detection. *Nat. Nanotechnol.* **5**, 391–400 (2010).
4. K.-J. Baeg, M. Binda, D. Natali, M. Caironi, Y.-Y. Noh, Organic light detectors: Photodiodes and phototransistors. *Adv. Mater.* **25**, 4267–4295 (2013).
5. H. Park, Y. Dan, K. Seo, Y. J. Yu, P. K. Duane, M. Wober, K. B. Crozier, Filter-free image sensor pixels comprising silicon nanowires with selective color absorption. *Nano Lett.* **14**, 1804–1809 (2014).
6. T. Xu, Y.-K. Wu, X. Luo, L. J. Guo, Plasmonic nanoresonators for high-resolution colour filtering and spectral imaging. *Nat. Commun.* **1**, 59 (2010).
7. Z. Zhao, C. Xu, Y. Ma, K. Yang, M. Liu, X. Zhu, Z. Zhou, L. Shen, G. Yuan, F. Zhang, Ultraviolet narrowband photomultiplication type organic photodetectors with Fabry–Pérot resonator architecture. *Adv. Funct. Mater.* **32**, 2203606 (2022).
8. A. Armin, R. D. Jansen-van Vuuren, N. Kopidakis, P. L. Burn, P. Meredith, Narrowband light detection via internal quantum efficiency manipulation of organic photodiodes. *Nat. Commun.* **6**, 6343 (2015).
9. B. Xie, R. Xie, K. Zhang, Q. Yin, Z. Hu, G. Yu, F. Huang, Y. Cao, Self-filtering narrowband high performance organic photodetectors enabled by manipulating localized Frenkel exciton dissociation. *Nat. Commun.* **11**, 2871 (2020).
10. K. Xia, Y. Li, Y. Wang, L. Portilla, V. Pecunia, Narrowband-absorption-type organic photodetectors for the far-red range based on fullerene-free bulk heterojunctions. *Adv. Opt. Mater.* **8**, 1902056 (2020).
11. Q. Lin, A. Armin, P. L. Burn, P. Meredith, Filterless narrowband visible photodetectors. *Nat. Photonics* **9**, 687–694 (2015).
12. Y. Fang, Q. Dong, Y. Shao, Y. Yuan, J. Huang, Highly narrowband perovskite single-crystal photodetectors enabled by surface-charge recombination. *Nat. Photonics* **9**, 679–686 (2015).
13. J. Wang, S. Xiao, W. Qian, K. Zhang, J. Yu, X. Xu, G. Wang, S. Zheng, S. Yang, Self-driven perovskite narrowband photodetectors with tunable spectral responses. *Adv. Mater.* **33**, 2005557 (2021).
14. J. Li, J. Wang, J. Ma, H. Shen, L. Li, X. Duan, D. Li, Self-trapped state enabled filterless narrowband photodetections in 2D layered perovskite single crystals. *Nat. Commun.* **10**, 806 (2019).
15. F. Guo, B. Yang, Y. Yuan, Z. Xiao, Q. Dong, Y. Bi, J. Huang, A nanocomposite ultraviolet photodetector based on interfacial trap-controlled charge injection. *Nat. Nanotechnol.* **7**, 798–802 (2012).
16. Y. Ma, X. Zhao, X. Xu, W. Wei, L. Shen, Ultralow dark current and high on–off ratio of perovskite photodetectors enabled by 3D/2D/3D heterostructures unipolar barrier. *Appl. Phys. Lett.* **123**, 231105 (2023).
17. S.-H. Liao, H.-J. Jhuo, Y.-S. Cheng, S.-A. Chen, Fullerene derivative-doped zinc oxide nanofilm as the cathode of inverted polymer solar cells with low-bandgap polymer (PTB7-Th) for high performance. *Adv. Mater.* **25**, 4766–4771 (2013).
18. J. Wang, P. Xue, Y. Jiang, Y. Huo, X. Zhan, The principles, design and applications of fused-ring electron acceptors. *Nat. Rev. Chem.* **6**, 614–634 (2022).
19. R. Dong, Y. Fang, J. Chae, J. Dai, Z. Xiao, Q. Dong, Y. Yuan, A. Centrone, X. C. Zeng, J. Huang, High-gain and low-driving-voltage photodetectors based on organolead triiodide perovskites. *Adv. Mater.* **27**, 1912–1918 (2015).
20. Z. Chen, Q. Dong, Y. Liu, C. Bao, Y. Fang, Y. Lin, S. Tang, Q. Wang, X. Xiao, Y. Bai, Y. Deng, J. Huang, Thin single crystal perovskite solar cells to harvest below-bandgap light absorption. *Nat. Commun.* **8**, 1890 (2017).
21. A. M. Ulatowski, A. D. Wright, B. Wenger, L. R. V. Buizza, S. G. Motti, H. J. Eggimann, K. J. Savill, J. Borchert, H. J. Snaith, M. B. Johnston, L. M. Herz, Charge-carrier trapping dynamics in bismuth-doped thin films of $MAPbBr_3$ perovskite. *J. Phys. Chem. Lett.* **11**, 3681–3688 (2020).
22. P. K. Nayak, M. Sendner, B. Wenger, Z. Wang, K. Sharma, A. J. Ramadan, R. Lovrinčić, A. Pucci, P. K. Madhu, H. J. Snaith, Impact of Bi^{3+} heterovalent doping in organic–inorganic metal halide perovskite crystals. *J. Am. Chem. Soc.* **140**, 574–577 (2018).
23. Z. Wang, B. Jia, G. Cai, J. Wang, Y. Li, P. Xue, X. Lu, Y. Lin, G. Wang, X. Zhan, Pyrrolo[3,2-*b*] pyrrole-based fused-ring electron acceptors with strong near-infrared absorption beyond 1000 nm. *Dyes Pigm.* **195**, 109705 (2021).
24. T. Li, G. Cai, Y. Lin, X. Lu, X. Zhan, Effects of thieno[3,2-*b*]thiophene number on narrow-bandgap fused-ring electron acceptors. *Chin. J. Polym. Sci.* **40**, 914–920 (2022).
25. T. Li, S. Dai, Z. Ke, L. Yang, J. Wang, C. Yan, W. Ma, X. Zhan, Fused tris(thienothiophene)-based electron acceptor with strong near-infrared absorption for high-performance as-cast solar cells. *Adv. Mater.* **30**, 1705969 (2018).
26. X. Zhang, X. Wu, X. Liu, G. Chen, Y. Wang, J. Bao, X. Xu, X. Liu, Q. Zhang, K. Yu, W. Wei, J. Liu, J. Xu, H. Jiang, P. Wang, X. Wang, Heterostructural $CsPbX_3$-PbS (X = Cl, Br, I) quantum dots with tunable Vis–NIR dual emission. *J. Am. Chem. Soc.* **142**, 4464–4471 (2020).
27. S. D. Stranks, G. E. Eperon, G. Grancini, C. Menelaou, M. J. P. Alcocer, T. Leijtens, L. M. Herz, A. Petrozza, H. J. Snaith, Electron-hole diffusion lengths exceeding 1 micrometer in an organometal trihalide perovskite absorber. *Science* **342**, 341–344 (2013).
28. Y. Yang, D. P. Ostrowski, R. M. France, K. Zhu, J. van de Lagemaat, J. M. Luther, M. C. Beard, Observation of a hot-phonon bottleneck in lead-iodide perovskites. *Nat. Photonics* **10**, 53–59 (2016).
29. S. Nah, B. Spokoyny, C. Stoumpos, C. M. M. Soe, M. Kanatzidis, E. Harel, Spatially segregated free-carrier and exciton populations in individual lead halide perovskite grains. *Nat. Photonics* **11**, 285–288 (2017).
30. Q. A. Alsulami, B. Murali, Y. Alsinan, M. R. Parida, S. M. Aly, O. F. Mohammed, Remarkably high conversion efficiency of inverted bulk heterojunction solar cells: From ultrafast laser spectroscopy and electron microscopy to device fabrication and optimization. *Adv. Energy Mater.* **6**, 1502356 (2016).
31. Y. Jiang, C. Qin, M. Cui, T. He, K. Liu, Y. Huang, M. Luo, L. Zhang, H. Xu, S. Li, J. Wei, Z. Liu, H. Wang, G.-H. Kim, M. Yuan, J. Chen, Spectra stable blue perovskite light-emitting diodes. *Nat. Commun.* **10**, 1868 (2019).
32. T. Leijtens, G. E. Eperon, A. J. Barker, G. Grancini, W. Zhang, J. M. Ball, A. R. S. Kandada, H. J. Snaith, A. Petrozza, Carrier trapping and recombination: The role of defect physics in enhancing the open circuit voltage of metal halide perovskite solar cells. *Energy Environ. Sci.* **9**, 3472–3481 (2016).
33. P. Calado, A. M. Telford, D. Bryant, X. Li, J. Nelson, B. C. O'Regan, P. R. F. Barnes, Evidence for ion migration in hybrid perovskite solar cells with minimal hysteresis. *Nat. Commun.* **7**, 13831 (2016).
34. J. Xu, A. Buin, A. H. Ip, W. Li, O. Voznyy, R. Comin, M. Yuan, S. Jeon, Z. Ning, J. J. McDowell, P. Kanjanaboos, J.-P. Sun, X. Lan, L. N. Quan, D. H. Kim, I. G. Hill, P. Maksymovych, E. H. Sargent, Perovskite–fullerene hybrid materials suppress hysteresis in planar diodes. *Nat. Commun.* **6**, 7081 (2015).
35. I. Levine, A. Al-Ashouri, A. Musiienko, H. Hempel, A. Magomedov, A. Drevilkauskaite, V. Getautis, D. Menzel, K. Hinrichs, T. Unold, S. Albrecht, T. Dittrich, Charge transfer rates and electron trapping at buried interfaces of perovskite solar cells. *Joule* **5**, 2915–2933 (2021).
36. V. M. Le Corre, E. A. Duijnstee, O. El Tambouli, J. M. Ball, H. J. Snaith, J. Lim, L. J. A. Koster, Revealing charge carrier mobility and defect densities in metal halide perovskites via space-charge-limited current measurements. *ACS Energy Lett.* **6**, 1087–1094 (2021).

37. J. Jiang, M. Xiong, K. Fan, C. Bao, D. Xin, Z. Pan, L. Fei, H. Huang, L. Zhou, K. Yao, X. Zheng, L. Shen, F. Gao, Synergistic strain engineering of perovskite single crystals for highly stable and sensitive X-ray detectors with low-bias imaging and monitoring. *Nat. Photonics* **16**, 575–581 (2022).
38. M. I. Saidaminov, V. Adinolfi, R. Comin, A. L. Abdelhady, W. Peng, I. Dursun, M. Yuan, S. Hoogland, E. H. Sargent, O. M. Bakr, Planar-integrated single-crystalline perovskite photodetectors. *Nat. Commun.* **6**, 8724 (2015).
39. Q. Dong, Y. Fang, Y. Shao, P. Mulligan, J. Qiu, L. Cao, J. Huang, Electron-hole diffusion lengths > 175 μm in solution-grown $CH_3NH_3PbI_3$ single crystals. *Science* **347**, 967–970 (2015).
40. D. Shi, V. Adinolfi, R. Comin, M. Yuan, E. Alarousu, A. Buin, Y. Chen, S. Hoogland, A. Rothenberger, K. Katsiev, Y. Losovyj, X. Zhang, P. A. Dowben, O. F. Mohammed, E. H. Sargent, O. M. Bakr, Low trap-state density and long carrier diffusion in organolead trihalide perovskite single crystals. *Science* **347**, 519–522 (2015).
41. A. Hwang, M. Park, Y. Park, Y. Shim, S. Youn, C.-H. Lee, H. B. Jeong, H. Y. Jeong, J. Chang, K. Lee, G. Yoo, J. Heo, Visible and infrared dual-band imaging via Ge/MoS_2 van der Waals heterostructure. *Sci. Adv.* **7**, eabj2521 (2021).
42. H. Wei, Y. Fang, P. Mulligan, W. Chuirazzi, H.-H. Fang, C. Wang, B. R. Ecker, Y. Gao, M. A. Loi, L. Cao, J. Huang, Sensitive X-ray detectors made of methylammonium lead tribromide perovskite single crystals. *Nat. Photonics* **10**, 333–339 (2016).
43. X. Pan, J. Zhang, H. Zhou, R. Liu, D. Wu, R. Wang, L. Shen, L. Tao, J. Zhang, H. Wang, Single-layer ZnO hollow hemispheres enable high-performance self-powered perovskite photodetector for optical communication. *Nanomicro Lett.* **13**, 70 (2021).
44. Y. Zhao, C. Li, J. Jiang, B. Wang, L. Shen, Sensitive and stable tin–lead hybrid perovskite photodetectors enabled by double-sided surface passivation for infrared upconversion detection. *Small* **16**, e2001534 (2020).
45. C. Li, H. Wang, F. Wang, T. Li, M. Xu, H. Wang, Z. Wang, X. Zhan, W. Hu, L. Shen, Ultrafast and broadband photodetectors based on a perovskite/organic bulk heterojunction for large-dynamic-range imaging. *Light Sci. Appl.* **9**, 31 (2020).
46. H. Haas, L. Yin, Y. Wang, C. Chen, What is LiFi? *J. Lightwave Technol.* **34**, 1533–1544 (2016).
47. M. Ayyash, H. Elgala, A. Khreishah, V. Jungnickel, T. Little, S. Shao, M. Rahaim, D. Schulz, J. Hilt, R. Freund, Coexistence of WiFi and LiFi toward 5G: Concepts, opportunities, and challenges. *IEEE Commun. Mag.* **54**, 64–71 (2016).
48. D. Li, J. Yang, M. Fang, B. Z. Tang, Z. Li, Stimulus-responsive room temperature phosphorescence materials with full-color tunability from pure organic amorphous polymers. *Sci. Adv.* **8**, eabl8392 (2022).
49. G. Tan, S. Wang, J. Yu, J. Chen, D. Liao, M. Liu, A. Nezamzadeh-Ejhieh, Y. Pan, J. Liu, Detection mechanism and the outlook of metal-organic frameworks for the detection of hazardous substances in milk. *Food Chem.* **430**, 136934 (2024).
50. F. Fernandes, A. Ashikhmin, T. L. Marzetta, Inter-cell interference in noncooperative TDD large scale antenna systems. *IEEE J. Sel. Areas Commun.* **31**, 192–201 (2013).
51. P. Stenumgaard, D. Persson, E. G. Larsson, K. Wiklundh, An early-warning service for emerging communication problems in security and safety applications. *IEEE Commun. Mag.* **51**, 186–192 (2013).

Acknowledgments

Funding: L.S. and W.W. thank the National Natural Science Foundation of China (T2425017, 62475094, and 62305128), the International Cooperation and Exchange Project of Jilin Province (20210402079GH and 20230402056GH), the 19th batch of innovative and entrepreneurial talent projects in Jilin Province (2023QN01), the Project of Science and Technology Development Plan of Jilin Province (grant no. 20220508037RC), and Graduate Innovation Fund of Jilin University. X.Zhan thanks the National Natural Science Foundation of China (grant no. 22335001). **Author contributions:** L.S. and X.Zhan conceived the idea and supervised the project. Y.M. systematically contributed to the photodetector fabrication and photoelectronic measurements. X.X. grew the perovskite single crystals and carried out SEM measurements. T.L., Z.W., and N.L. synthesized 5TTIC, PPIC2, and FOIC. X.Zhao measured the EQE. W.W. contributed to discussions and assisted the research. All authors discussed the results and commented on the manuscript. **Competing interests:** The authors declare that they have no competing interests. **Data and materials availability:** All data needed to evaluate the conclusions in the paper are present in the paper and/or the Supplementary Materials.

Submitted 27 April 2024
Accepted 24 April 2025
Published 30 May 2025
10.1126/sciadv.adq1127